Supporting Information
For

A Six-Coordinate Peroxynitrite Low-Spin Iron(III) Porphyrinate Complex – The Product of the Reaction of Nitrogen Monoxide (•NO$_{(g)}$) with a Ferric-Superoxide Species

Savita K. Sharma, [†] Andrew W. Schaefer, [‡] Hyeongtaek Lim,[‡] Hirotoshi Matsumura,[§] Pierre Moënne-Loccoz,[§] Britt Hedman,[ǁ] Keith O. Hodgson,[‡,ǁ] Edward I. Solomon,*[‡,ǁ] and Kenneth D. Karlin*[†]

[†]Johns Hopkins University, Baltimore, Maryland 21218, USA

[‡]Department of Chemistry, Stanford University, Stanford, California 94305, USA

[§]Division of Environmental & Biomolecular Systems & Science University, Portland, OR 97239-3098, USA

[ǁ]Stanford Synchrotron Radiation Lightsource, SLAC National Accelerator Laboratory, Stanford University, Menlo Park, California 94025, USA

Table of Contents

I. General procedures

II. Synthetic procedures

a) Synthesis of $[(P^{Im})Fe^{III}](NO_3).THF$ (**4b**) and d_8-(**4b**)

b) Synthesis of $(P^{Im})Fe^{III}$-OH (**5**) and d_8-(**5**)

c) Synthesis of $[(P^{Im})Fe^{III}](SbF_6)$ (**6**) and d_8-(**6**)

d) Generation of Compound II and its reaction with $\cdot NO_{2(g)}$: UV-Vis experiment

e) Analysis of Nitrate ion by Capillary Electrophoresis

f) Nitration of the 2,4-di-tert-butylphenol (^{2,4}DTBP)

III. Reaction Scheme: Scheme S1: Sequence of reaction showing the formation of ferric superoxo complex **2** by bubbling dioxygen gas through the THF solution of complex **1** at -80 °C. Excess $O_{2(g)}$ was removed by three vac/Ar purge cycle, to this added $NO_{(g)}$ to generate an intermediate species **3** (ferric-Peroxynitrite), excess NO(g) was removed by several vac/Ar purge cycle. At low temperature, complex **3** is stable only for few minutes and decomposed to complex **4a** (6-coordinate nitrato complex) and at room temperature it forms five coordinate complex **4b**.

IV. Spectroscopic characterizations

Figure S1. The spectroscopic feature of authentic complex $[(P^{Im})Fe^{III}](NO_3)$ (**4b**) in THF. (A) UV-Vis; (B) ^{2}H NMR (46.05 MHz; * indicates the solvent peak THF) and (C) X-band EPR recorded at 14 K (2 mM of **4b** in THF: g = 5.98, 1.98).

Figure S2. UV-Vis, ^{2}H NMR and X-band EPR of $(P^{Im})Fe^{III}$-OH (**5**) in THF. EPR recorded at 14 K while UV-Vis and NMR at RT.

Figure S3. The spectroscopic feature of complex $[(P^{Im})Fe^{III}](SbF_6)$ (**6**) in THF. (A) UV-Vis; (B) ^{2}H NMR (46.05 MHz; * indicates the solvent peak THF) and (C) X-band EPR recorded at 14 K (2 mM of **6** in THF: g = 6.01, 1.98).

Figure S4. rRaman spectra of complexes $[(P^{Im})Fe^{III}-(O_2^{\cdot-})]$ (**2**, **red**), $[(P^{Im})Fe^{III}-(^-OON=O)]$ (**3**, **green**) and $[(P^{Im})Fe^{III}-(NO_3^-)]$ (**4a**, grey) collected at 413.1 nm (top right) and 457.9 nm (top, left); rRaman spectra of $[(P^{Im})Fe^{III}-(O_2^{\cdot-})]$ (**2**) collected at 413 nm (bottom, right) and $[(P^{Im})Fe^{II}-NO]$ (bottom, left) collected at 442 nm.

Figure S5. X-band EPR spectra (left) of complex **3** (**green**) which decays to complex **4b** (**grey**) in the reaction sequence described in the main text; (right) showing the EPR spectrum of (i) *in situ* generated complex $[(P^{Im})Fe^{III}(^-OON=O)]$ (**3**) (top, **green**, 2 mM), (ii) an authentic low-spin iron(III) complex $[(F_8)Fe^{III}(DCHIm)_2]$ (middle, **red**, 2 mM) and where DCHIm is 1,5-dicyclohexyl imidazole, and (iii) the authentic high-spin iron(III) complex $[(F_8)Fe^{III}-OH]$ (bottom, **black**, 2 mM). One can readily see from the relative intensities of signals at g = 5.97, that this low field signal in the peroxynitrite spectrum (top) is in fact a rather weak signal, representing only 5-10% of the paramagnetic material in the solution, most probably being $[(P^{Im})Fe^{III}-OH]$ (**5**) (see above, Figure S2), the close analog of $[(F_8)Fe^{III}-OH]$.

Figure S6. The comparison of *in situ* generated $[(P^{Im})Fe^{III}(^-OON=O)]$ (**3**) (**green**) to nitrato complex (**4**) generated *in situ* (via thermal decay of **3**) (**brown**), and isolated nitrato complex $[(P^{Im})Fe^{III}](NO_3)$ (formed by addition of excess ($nBu_4N^+NO_3^-$) to $[(P^{Im})Fe^{III}](SbF_6)$ (**6**)) (**grey**). These spectra show that there can be two forms of the P^{Im}-Fe(III)-

nitrato complex, low-spin $[(P^{Im})Fe^{III}(NO_3)]$ (**4a**) and high-spin $[(P^{Im})Fe^{III}](NO_3)$ **4b**, and that there are features arising from LS Fe(III) that are present in **3** but absent in **4a** and **4b** (note that the precursor, $[(P^{Im})Fe^{III}-(O_2^-)]$ (**2**), is EPR silent). This indicates that **3** is distinct from either nitrato species. Additionally, attempts to generate **4a** at low temperature resulted in a mixture of low-spin (**4a**) and high-spin (**4b**) nitrato compounds, with the low-spin component never exceeding 50% of the mixture. The spectrum for complex **3** shows only 5-10% high-spin heme (the rest is low-spin), indicating that any low-spin nitrato present in **3** must comprise less than 5-10% of the total sample, with the remainder representing a distinct low-spin species.

Figure S7. The spectroscopic features of *in situ* generated nitrito iron(III) complex $[(P^{Im})Fe^{III}(NO_2)]$ by the addition of excess $(nBu_4N^+NO_2^-)$ to $[(P^{Im})Fe^{III}](SbF_6)$ (**6**); (left) UV-Vis spectrum; (right) X-band EPR spectrum recorded at 14 K (2 mM, THF). One purpose of showing these spectra is to show, that our putative peroxynitrite complex **3** is completely different from *in situ* generated iron(III) nitrito complex.

Figure S8. The UV-Vis spectrum (left, inset) compd II $[(P^{Im})Fe^{IV}=O]$ (**7**) (**red**) generated *in situ* by the addition of *m*CPBA to complex **1** (**black**); (left) addition of $\bullet NO_{2(g)}$ to the fully formed compd II (**red**) resulted in the generation of iron(III) nitrate **4a** (**green**) to **grey 4b**. The X-band EPR (THF, 14 K) spectrum (right) complex **1** and **7** (compd II, **black**) are EPR inactive, addition of $\bullet NO_{2(g)}$ to **7** gives and adduct (**green**) which finally coverts to complex **4b** (**brown**).

Figure S9: The UV-Vis spectrum (overlay, left) of ferrous nitrosyl (**blue**) and ferric nitrosyl (**black**) generated at -80 °C in THF. (right) EPR of frozen ferrous nitrosyl while ferric nitrosyl is EPR silent. Note: Our ferrous nitrosyl complex is very stable at room temperature, we can isolate as solid while ferric-nitrosyl species we can only generate and stable at low temperatures. One purpose of showing these spectra is to show, that our putative peroxynitrite species **3** as well decomposed species are completely different than what we are observing in the present chemistry.

V. XAS study

Figure S10. Fe K-edge EXAFS data (left) and non-phase-shift-corrected Fourier transforms (right) of complex **2** (**red**), **3** (**green**), **4a** (**grey**), and **5** (**blue**).

Figure S11. Fe K-edge EXAFS data and non-phase-shift-corrected Fourier transforms of complex (A) **2**, (B) **3**, (C) **4a**, and (D) **5**. Data (—) and fits (---).

Table S1. XAS Pre-edge Energies and Intensities.

Table S2. EXAFS Fitting Results.

VI. DFT calculations

Figure S12. Summary of overall thermodynamics calculated using DFT, including structures with and without phenol. Note that the computational model used unsubstituted phenol, while [2,4]DTBP was used experimentally.

Table S3. Optimized DFT PN Conformations.

VII. References

I. General procedures

All reagents and solvents were purchased from commercial sources and were of reagent quality unless otherwise stated. Air-sensitive compounds were handled under an argon atmosphere by using standard Schlenk techniques or in an MBraun Labmaster 130 inert atmosphere (<1 ppm O_2, <1 ppm H_2O) glovebox filled with nitrogen. Pentane was distilled over calcium hydride under argon, whereas toluene and dichloromethane (CH_2Cl_2) were purified over activated alumina columns under nitrogen. The tetrahydrofuran (THF) was purified over sodium metal/benzophenone. Deoxygenation of these solvents was achieved by bubbling with argon for 30 min or by three freeze/pump/thaw cycles prior to introduction into the glovebox.

Benchtop UV-Vis experiments were carried out using Hewlett-Packard 8453 diode array spectrophotometer equipped with a HP-Chem-Station software, where the spectrophotometer was equipped with a liquid nitrogen chilled Unisoku USP-203-A cryostat. ^{1}H NMR spectra at room temperature were recorded on a Bruker 300 NMR instrument. Variable temperature and ^{2}HNMRspectroscopic studies were carried out on a Bruker 300 NMR instrument (^{1}H at 300 MHz, ^{2}H at 46.05 MHz). All spectra were recorded in 5-mm o.d.NMR tubes. The chemical shifts were reported as δ (ppm) values calibrated to natural abundance deuterium or proton solvent peaks. A tunable broadband probe was used in collecting ^{2}H NMR spectra. Typically, 0.5 mL of 2-3 mM of respective complex solution were used for each experiment. Electron paramagnetic resonance (EPR) spectra were recorded with a Bruker EMX spectrometer equipped with a Bruker ER 041 X G microwave bridge and a continuous-flow liquid helium cryostat (ESR900) coupled to an Oxford Instruments TC503 temperature controller. Spectra were obtained at 14 K under nonsaturating microwave power conditions (ν = 9.4108 GHz, microwave power = 0.201 mW, modulation amplitude = 10 G, microwave frequency = 100 kHz, receiver gain = 5.02×10^3). Gas chromatography (GC) was performed on an Agilent 6890 gas chromatography fitted with HP-5 (5% - phenyl)-methylpolysiloxane capillary column (30 m * 0.32 mm* 0.25 mm) and equipped with a flame ionization detector. The GC-FID response factors for 2-nitrophenol and 2,4-di-*tert*-butylphenol were prepared vs. dodecane as an internal standard. Elemental analysis were performed by Desert Analytics, Tucson, AZ.

II. Synthetic procedure

a) Synthesis of [(P^{Im})Fe^{III}](NO$_3^-$).THF 4b. (P^{Im})Fe^{III}-OH (**5**), reported previously[1] (0.100 g, 0.1 mM) was dissolved in 80 mL of THF at room temperature in the dry box. To this solution AgNO$_3$ (0.85 g, 0.5 mM) was added and allowed to stir overnight. The solvent was removed under vacuum and the resulted purplish-brown solid obtained was redissolved in CH_2Cl_2, filtered over celite to remove the inorganic salts (AgOH). DCM solution was layered with pentane to obtain purified material. Micro crystalline material were collected (0.083 g, 86% yield) of [(P^{Im})Fe^{III}](NO$_3^-$) **4b**. The UV-Vis spectra (λ_{max}, THF, nm): 414, 500 (sh), 527, 576 (sh), 636, 670 nm. ^{2}H NMR (46.05 MHz, THF-d_8, δ ppm): 34.05, 42.10 and 51.49. Elemental analysis**:** (C$_{60}$H$_{43}$N$_8$F$_6$FeO$_5$) Calculated: C (64.01), H (3.85), N (9.95); found: C (63.94), H (3.92), N (9.89). EPR spectrum**:** X-band (ν = 9.186 GHz) spectrometer (2 mM, THF, 14 K): g = 6.02, 1.99, (Figure S1).

Synthesis of d_8-[(P^{Im})Fe^{III}](NO$_3^-$) (d_8-4b): The pyrrole deuterated heme–Fe^{III} d_8-[(P^{Im})Fe^{III}](NO$_3^-$) was prepared using identical procedure to that described above for [(P^{Im})Fe^{III}](NO$_3^-$), but employing pyrrole deuterated porphyrin d_8-(P^{Im})Fe^{III}-OH[1,2] instead of (P^{Im})Fe^{III}-OH. ^{2}H NMR (46.05 MHz, THF, δ, ppm, RT): 34.05, 42.10 and 51.49 (pyrrole-D), (Figure S1).

b) Synthesis of [(P^{Im})Fe^{III}-OH (5)
Complex **5** and the deuterated complex d_8-**5** was prepared in a similar manner as previously reported earlier.[1] Figure S2, shows the spectroscopic features of complex **5** in THF. Complex **5** is one of the decay product of superoxo [(P^{Im})Fe^{III}-(O$_2^{-}$)] (**2**), see main text for details.

c) Synthesis of [(P^{Im})Fe^{III}](SbF$_6$) (6)
In a 50 mL Schlenk flask equipped with a stir bar added (P^{Im})Fe^{III}-OH (**5**) (0.137 g, 0.138 mM) and AgSbF$_6$ (0.072 g, 0.207 mM), dissolved in 20 mL of THF. Reaction flask was covered with aluminum foil and stirred overnight at

room temperature. The reaction mixture was filtered through celite to remove black precipitate (AgOH). The solvent THF was removed and crude material obtained was re-dissolve in DCM and layered with pentane to obtain pure shining crystalline material in 73% yield. UV-Vis (λ_{max}, THF, nm): 412, 502 (sh), 529, 656 (br). FTIR (ν_{SbF6}) = 654 cm^{-1}. ^{2}H NMR (46.05 MHz, THF, δ, ppm, RT): 43.84, 43.46, 42.33 (Pyrrole-D). Elemental analysis: ($C_{55}H_{32}N_8F_{12}FeOSb$) Calculated: C (54.48), H (2.66), N (8.09); found ($C_{55}H_{32}N_8F_{12}FeOSb.THF$): C (55.16), H (3.14), N (7.63). EPR spectrum: X-band (ν = 9.186 GHz) spectrometer (2 mM, THF, 14 K): g = 5.89, 1.98, (Figure S3).

d) Generation of Compound II and its reaction with •NO$_{2(g)}$: UV-Vis experiment

In the dry box, stock solution was prepared by dissolving complex **1** (0.002 g, 2 mM) in THF. In a Schlenk cuvette 3 mL of (P^{Im})Fe^{II} (**1**) (0.015 mM) (λ_{max} = 417, 525, 552 (sh) nm) was transferred and the cuvette was sealed by using rubber septa which was secured by copper wire inside the dry box. The Schlenk cuvette was transferred from the dry box to the pre cooled UV-Vis cryostat at -80 °C. To this solution 1.5 equivalent of mCPBA (7.8 mM in toluene) was added. Change in spectra was observed from **1** (λ_{max} = 417, 525 nm; Figure S8, **black** shown in inset) to (P^{Im})Fe^{IV}=O (**7**) or Compd II(λ_{max} = 420, 553 nm; **red** shown in inset)[1b] with an isobestic conversion. Addition of 1 mL of •NO$_2$ gas to *in situ* generated Compd II, resulted in immediate change in UV-Vis spectrum and form (P^{Im})Fe^{III}-NO$_3$ **4a** (λ_{max} = 414, 544 nm, **green**) at low temperature. Upon warming, the spectra changes to a typical five-coordinate species (**grey**, Figure S8) complex **4b**. The final product shows positive test for nitrate ion as well as closed match of UV-Vis, and EPR spectroscopy of Authentic complex **4b**.

e) Analysis of Nitrate ion by Capillary Electrophoresis

In the dry box, 10 mL Schlenk flask equipped with a magnetic stir bar added (P^{Im})Fe^{II} (0.004 g, 0.82 mM) and was dissolved in 5 mL of THF. Schlenk flask was taken out from the drybox and cooled at –80 ^{0}C (acetone/liq N2 bath). To this cold solution dry dioxygen (O$_2$) was bubbled to generate **2**. After five min excess dioxygen was removed by several cycles of Ar/Vacuum, followed by addition of •NO gas by using gas tight three-way long syringe needle to **2**. The excess •NO gas was removed by applying several cycles of Ar/vacuum. The reaction mixture was allowed to stir for an hour at low temperature. The solvent was then removed under vacuum and solid was redissolved in 10 mL CH$_2$Cl$_2$ and extracted with 10 mL of aqueous NaCl solution. The presence of significant amounts of nitrate ion in the aqueous layer was confirmed by semi quantitative QUANTOFIX nitrate/nitrite test strips as well as the UV-Vis spectrum showing a very broad band at ~ 300 nm corresponding to nitrate n —> π* transitions and a strong band at ~200 nm corresponding to π —> π*.[2] Later, capillary electrophoresis (CE) was used for nitrate[3] quantification in the aqueous layer. A standard calibration curve was first constructed using sodium nitrate. By employing optimal conditions, the calibration curve was generated for a concentration range of 100–500 μM. This nitrate analysis indicated nitrate (NO$_3^-$) ion was present in the product mixture with a yield of 94.2% (385 μM).
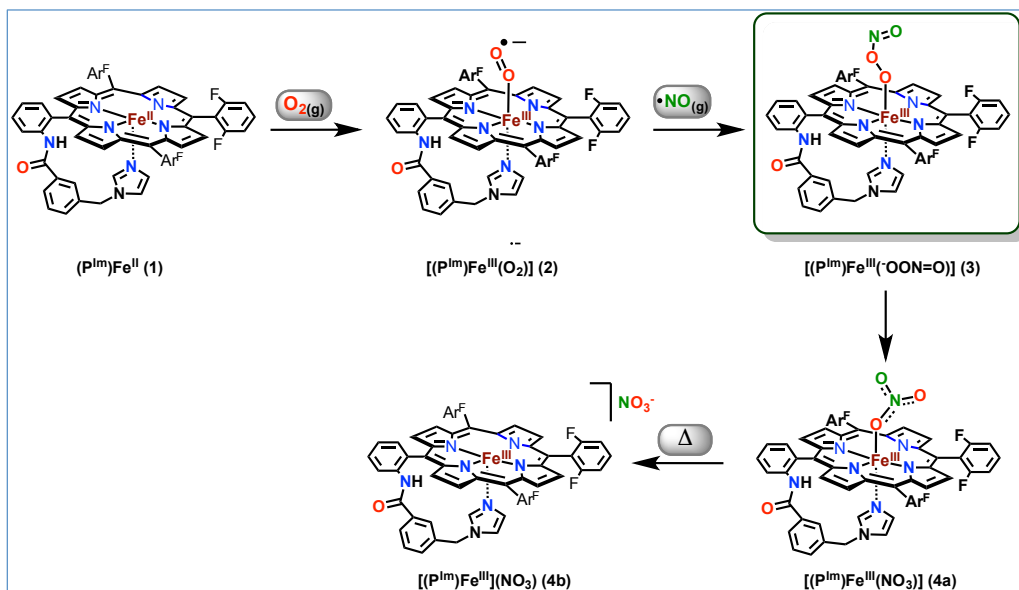
f) Nitration of the 2,4-Di-tert-butylphenol (^{2,4}DTBP).

The formation of the superoxo complex **2** in THF at - 80 °C was carried out as described in the main text from **1** (0.0021 g, 2.0 mM). Excess O$_{2(g)}$ was rigorously removed by bubbling the solution with Ar and vacuum purge cycles as before. Two equivalents of 2,4-di-tert-butylphenol (^{2,4}DTBP) (0.0011 g, 4.0 mM) were added from a stock solution of ^{2,4}DTBP in THF. Upon addition of the ^{2,4}DTBP no change in the UV-vis spectrum was observed. 1 mL ·NO$_{(g)}$ was added by using a gas tight three-way needle syringe. The solution was stirred at -80 °C for ten minutes before warming to room temperature. The reaction mixture was stirred at RT for 5-6 hours and then solution was concentrated in vacuum and pentane was added to precipitate the Fe product. The pentane solution was collected by decanting. The Fe product was washed several times with pentane, and the pentane solution was removed and collected by decanting after each wash. The solid Fe product was dried in vacuum, dissolved in THF and its UV-vis spectrum was recorded and looks like 5-coordinate Fe(III) (λ_{max} = 412 (Soret), 502 sh, 529 and 656 nm). The iron product shows negative results for nitrite/nitrate ion. The pentane solution containing the phenolic products was filtered to remove any trace of iron product and the solvent was injected in GC with internal standard dodocane, showed 2,4-di-*t*-butyl-6-nitrophenol (NO$_2$-DTBP) (85% yield) and unreacted ^{2,4}DTBP as the only products of the reaction. These were identified by comparison to the spectra obtained from commercial 2,4-di-*t*-butyl-6-nitrophenol, and 2,4-di-*t*-butylphenol respectively.

Warming [(P^{Im})Fe^{III}(NO$_3^-$)] (4a) in the Presence of ^{2,4}DTBP.

The complex [(P^{Im})Fe^{III}](NO$_3^-$) (**4b**) (0.003 g, 2.88 mM) was dissolved in deaerated THF and cooled to - 80 °C. Two equivalent of ^{2,4}DTBP (3.00 mmol) was added from a stock solution of ^{2,4}DTBP (10.0 mM) in THF. The solution was stirred for ten minutes at - 80 °C before warming to room temperature. After workup as described above, GC spectrum showed only unreacted ^{2,4}DTBP, and the isolated Fe product dissolved in THF showed only **4b**.

III. Reaction Scheme

Scheme S1: Sequence of reaction showing the formation of ferric superoxo complex **2** by bubbling dioxygen gas through the THF solution of complex **1** at -80 °C. Excess O$_{2(g)}$ was removed by three vac/Ar purge cycle, to this added NO$_{(g)}$ to generate an intermediate species **3** (ferric-Peroxynitrite), excess NO(g) was removed by several vac/Ar purge cycle. At low temperature, complex **3** is stable only for few minutes and decomposed to complex **4a** (6-coordinate nitrato complex) and at room temperature it forms five coordinate complex **4b**.
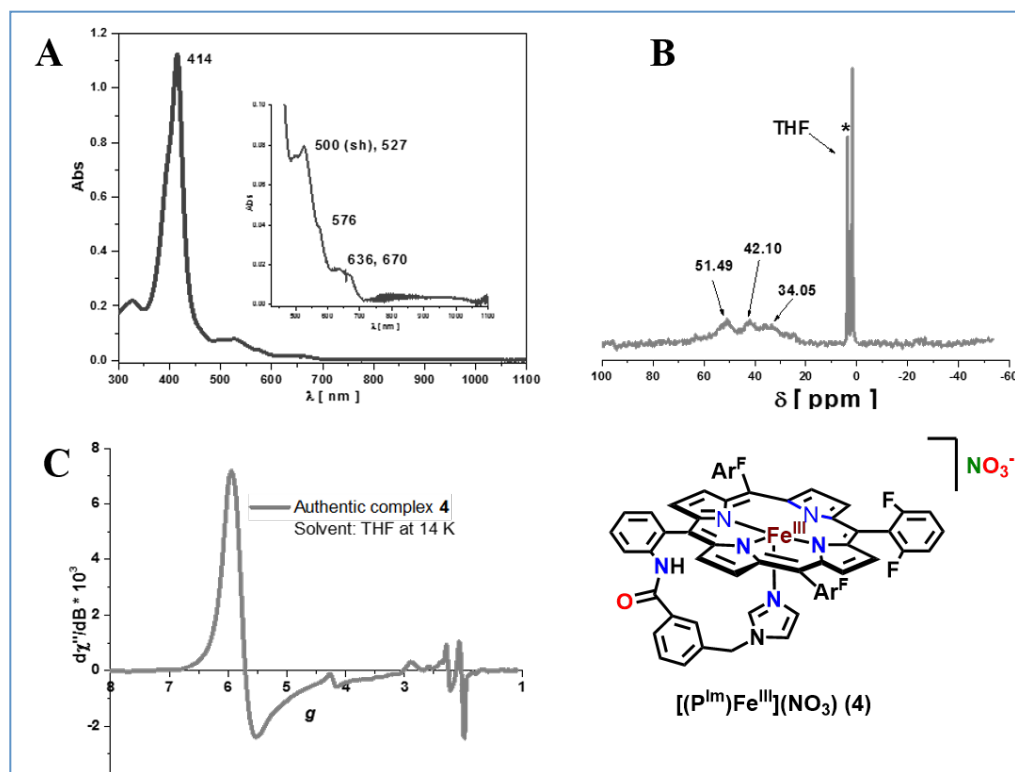
IV. Spectroscopic Characterizations

Figure S1. The spectroscopic feature of authentic complex $[(P^{Im})Fe^{III}](NO_3)$ (**4b**) in THF. (A) UV-Vis; (B) ^{2}H NMR (46.05 MHz; * indicates the solvent peak THF) and (C) X-band EPR recorded at 14 K (2 mM of **4b** in THF: g = 5.98, 1.98).
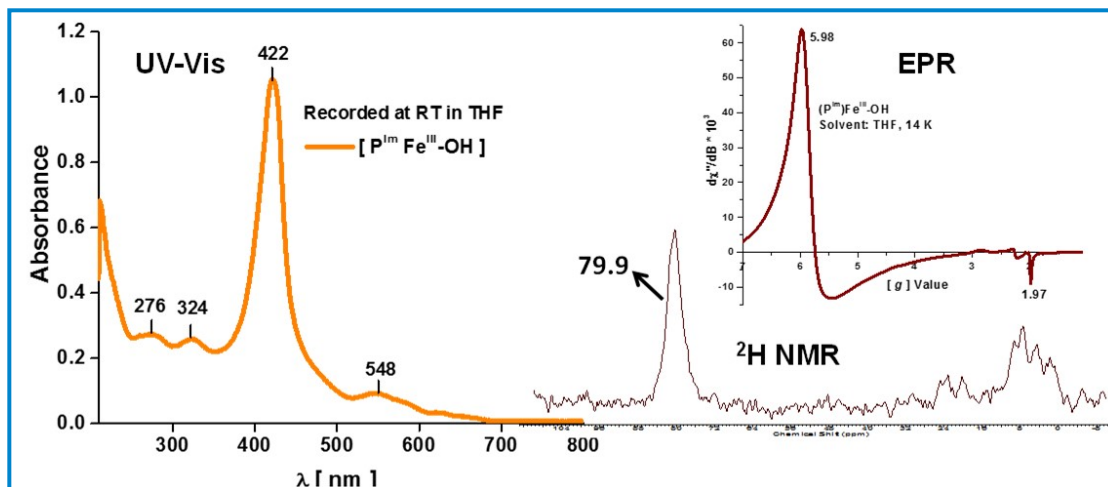

Figure S2. UV-Vis, ^{2}H NMR and X-band EPR of $(P^{Im})Fe^{III}$-OH (**5**) in THF. EPR recorded at 14 K while UV-Vis and NMR at RT.
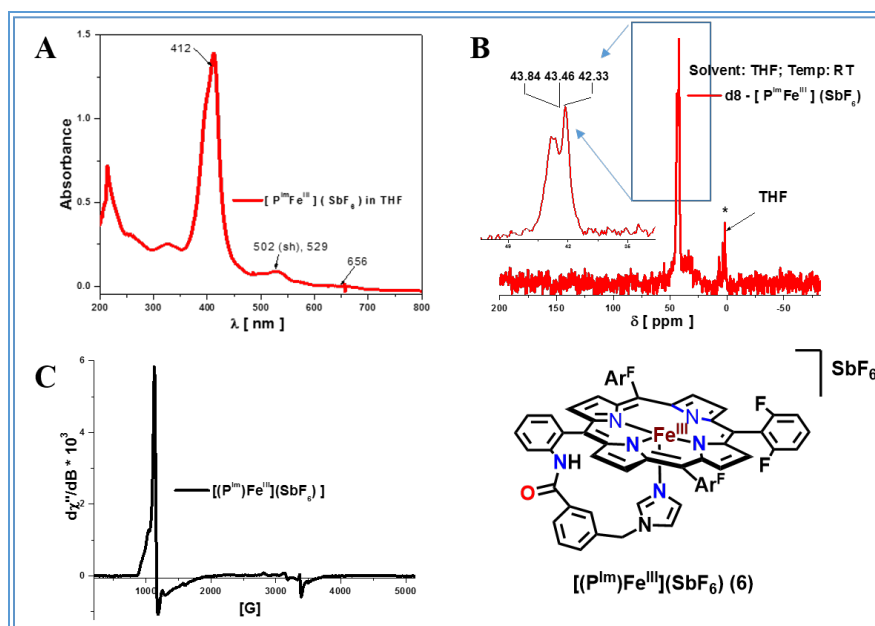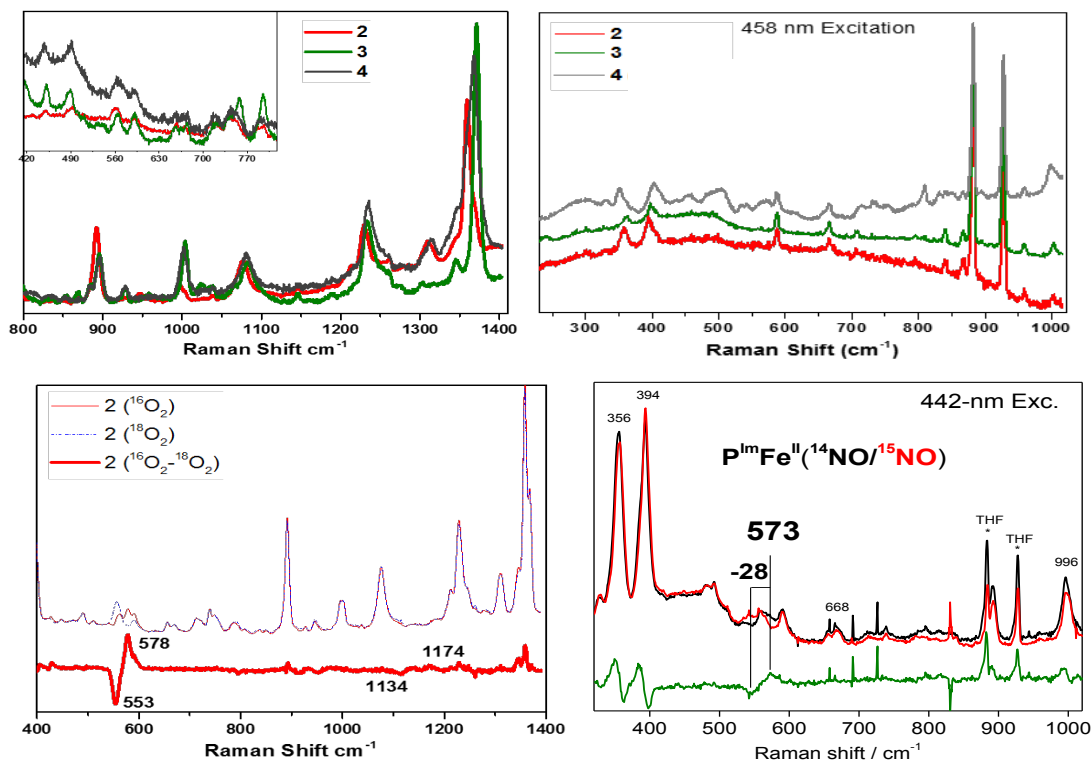
Figure S3. The spectroscopic feature of complex $[(P^{Im})Fe^{III}](SbF_6)$ (**6**) in THF. (A) UV-Vis; (B) ^{2}H NMR (46.05 MHz; * indicates the solvent peak THF) and (C) X-band EPR recorded at 14 K (2 mM of **6** in THF: g = 6.01, 1.98).

Figure S4. rRaman spectra of complexes $[(P^{Im})Fe^{III}\text{-}(O_2^-)]$ (**2**, **red**), $[(P^{Im})Fe^{III}\text{-}(^-OON=O)]$ (**3**, **green**) and $[(P^{Im})Fe^{III}\text{-}(NO_3^-)]$ (**4a**, grey) collected at 413.1 nm (top right) and 457.9 nm (top, left); rRaman spectra of $[(P^{Im})Fe^{III}\text{-}(O_2^-)]$ (**2**) collected at 413 nm (bottom, right) and $[(P^{Im})Fe^{II}\text{-}NO]$ (bottom, left) collected at 442 nm.
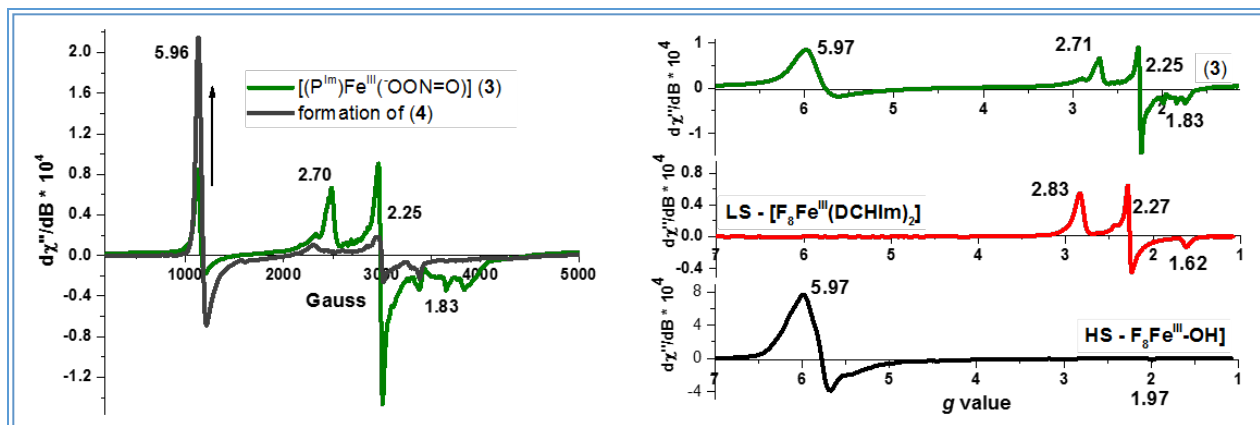
Figure S5. X-band EPR spectra (left) of complex **3** (**green**) which decays to complex **4b** (**grey**) in the reaction sequence described in the main text; (right) showing the EPR spectrum of (i) *in situ* generated complex $[(P^{Im})Fe^{III}(^-OON=O)]$ (**3**) (top, **green**, 2 mM), (ii) an authentic low-spin iron(III) complex $[(F_8)Fe^{III}(DCHIm)_2]$ (middle, **red**, 2 mM) and where DCHIm is 1,5-dicyclohexyl imidazole, and (iii) the authentic high-spin iron(III) complex $[(F_8)Fe^{III}-OH]$ (bottom, **black**, 2 mM). One can readily see from the relative intensities of signals at g = 5.97, that this low field signal in the peroxynitrite spectrum (top) is in fact a rather weak signal, representing only 5-10% of the paramagnetic material in the solution, most probably being $[(P^{Im})Fe^{III}-OH]$ (**5**) (see above, Figure S2),[1a] the close analog of $[(F_8)Fe^{III}-OH]$.[4]
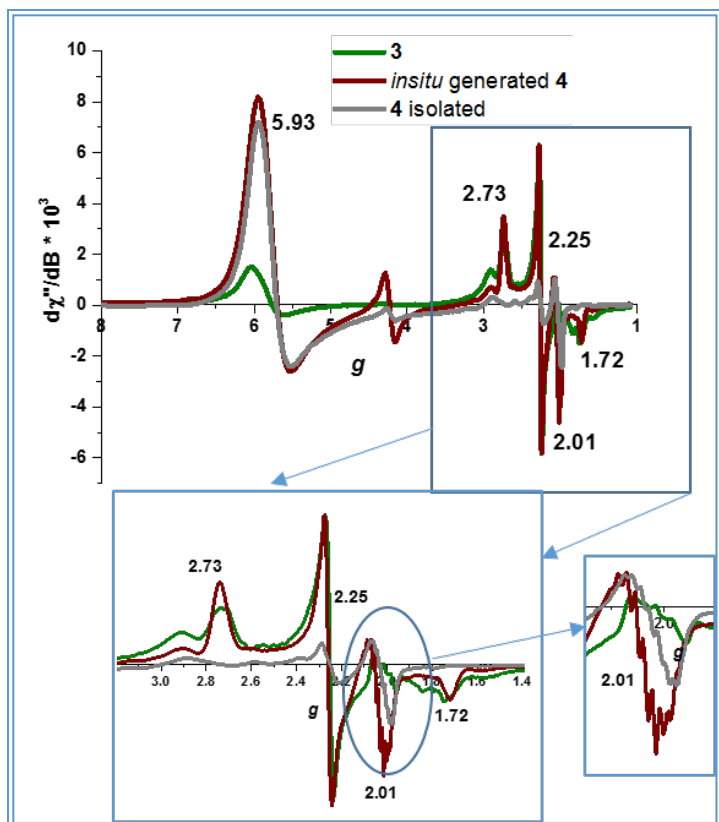
Figure S6. The comparison of *in situ* generated $[(P^{Im})Fe^{III}(^{-}OON=O)]$ (**3**) (**green**) to nitrato complex (**4**) generated *in situ* (via thermal decay of **3**) (**brown**), and isolated nitrato complex $[(P^{Im})Fe^{III}](NO_3)$ (formed by addition of excess $(nBu_4N^{+}NO_3^{-})$ to $[(P^{Im})Fe^{III}](SbF_6)$ (**6**)) (**grey**). These spectra show that there can be two forms of the P^{Im}-Fe(III)-nitrato complex, low-spin $[(P^{Im})Fe^{III}(NO_3)]$ (**4a**) and high-spin $[(P^{Im})Fe^{III}](NO_3)$ **4b**, and that there are features arising from LS Fe(III) that are present in **3** but absent in **4a** and **4b** (note that the precursor, $[(P^{Im})Fe^{III}-(O_2^{-})]$ (**2**), is EPR silent). This indicates that **3** is distinct from either nitrato species. Additionally, attempts to generate **4a** at low temperature resulted in a mixture of low-spin (**4a**) and high-spin (**4b**) nitrato compounds, with the low-spin component never exceeding 50% of the mixture. The spectrum for complex **3** shows only 5-10% high-spin heme (the rest is low-spin), indicating that any low-spin nitrato present in **3** must comprise less than 5-10% of the total sample, with the remainder representing a distinct low-spin species.
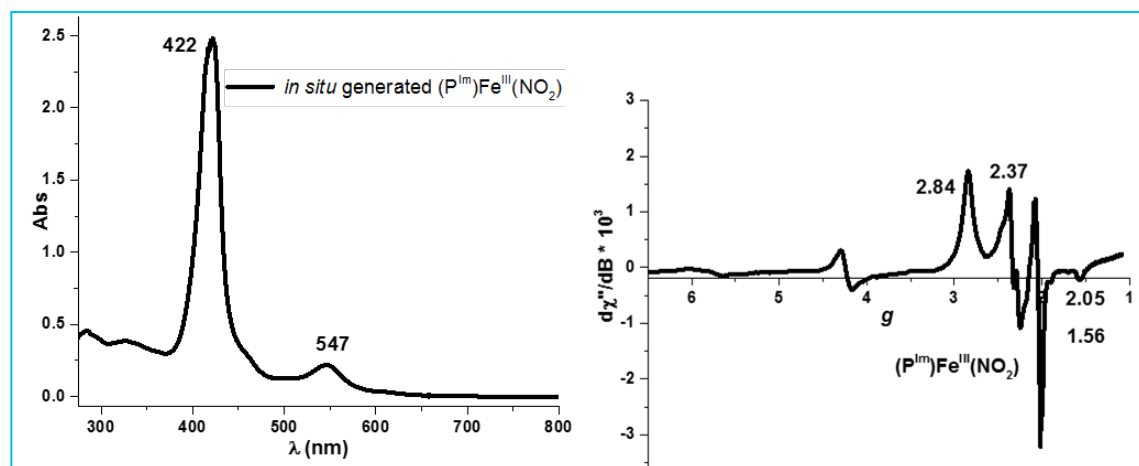
Figure S7. The spectroscopic features of *in situ* generated nitrito iron(III) complex $[(P^{Im})Fe^{III}(NO_2)]$ by the addition of excess $(nBu_4N^+NO_2^-)$ to $[(P^{Im})Fe^{III}](SbF_6)$ (**6**); (left) UV-Vis spectrum; (right) X-band EPR spectrum recorded at 14 K (2 mM, THF). <u>One purpose of showing these spectra is to show, that our putative peroxynitrite complex **3** is completely different from *in situ* generated iron(III) nitrito complex.</u>
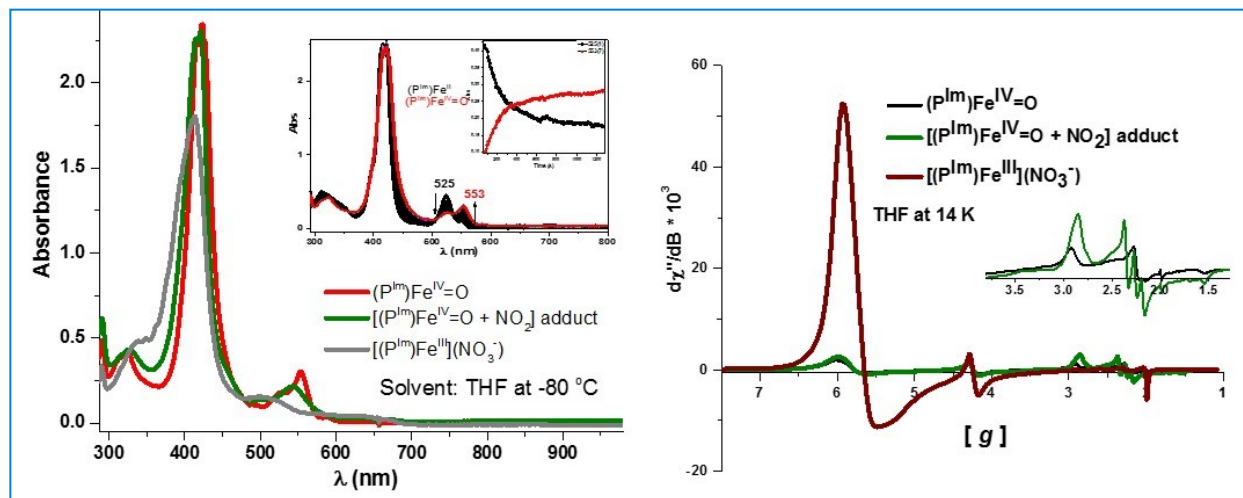

Figure S8. The UV-Vis spectrum (left, inset) compd II $[(P^{Im})Fe^{IV}=O]$ (**7**) (**red**) generated *in situ* by the addition of *m*CPBA to complex **1** (**black**); (left) addition of •$NO_{2(g)}$ to the fully formed compd II (**red**) resulted in the generation of iron(III) nitrate **4a** (**green**) to **grey 4b**. The X-band EPR (THF, 14 K) spectrum (right) complex **1** and **7** (compd II, **black**) are EPR inactive, addition of •$NO_{2(g)}$ to **7** gives and adduct (**green**) which finally coverts to complex **4b** (**brown**).
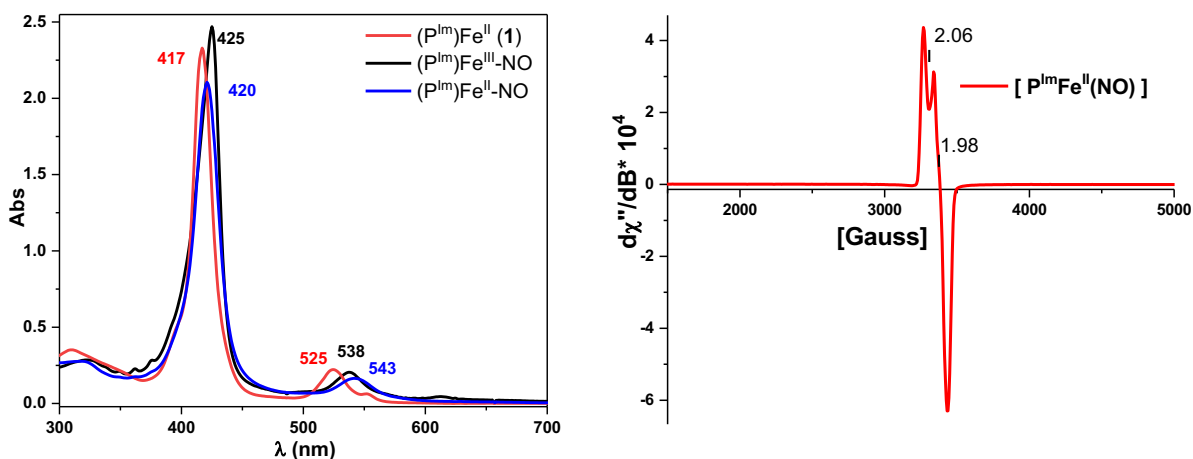

Figure S9: The UV-Vis spectrum (overlay, left) of ferrous nitrosyl[5] (**blue**) and ferric nitrosyl (**black**) generated at -80 °C in THF. (right) EPR of frozen ferrous nitrosyl[5] while ferric nitrosyl is EPR silent. Note: Our ferrous nitrosyl complex is very stable at room temperature, we can isolate as solid while ferric-nitrosyl species we can only generate and stable at low temperatures. One purpose of showing these spectra is to show, that our putative peroxynitrite species **3** as well decomposed species are completely different than what we are observing in the present chemistry.

V. XAS Study

XAS data analysis.

Photoreduction and photodegradation were hardly observed over the scans in the extended X-ray absorption fine structure (EXAFS) region and thus for EXAFS analysis all scans were used in the final average; the EXAFS data reported here include an average of 19, 26, 17, and 18 scans for complex $[(P^{Im})Fe^{III}(O_2^-)]$ (**2**), $[(P^{Im})Fe^{III}(^-OON=O)]$ (**3**), $[(P^{Im})Fe^{III}(NO_3)]$ (**4a**), and $[(P^{Im})Fe^{III}(OH)]$ (**5**), respectively.

Background subtraction and normalization of the data were performed using PySpline.[6] For EXAFS analysis, the data (k = 16 Å^{-1}) were processed by fitting a second-order polynomial to the pre-edge region and subtracting this from the entire spectrum as a background. A three-region polynomial spline of orders 2, 3, and 3 was used to model the smoothly decaying post-edge region. The data were normalized by scaling the spline function to an edge jump of 1.0 at 7130 eV. For edge and pre-edge analysis, the full data sets were truncated to k = 9.5 Å^{-1} and reprocessed using a second-order polynomial background and a one-region spline of order 2 for comparison between the current data sets and the data of past reference compounds.[7]

The Fe K pre-edge features were modeled with pseudo-Voigt line shapes with a 1:1 ratio of Lorentzian:Gaussian functions using the fitting program EDG_FIT (George, G. N. Stanford Synchrotron Radiation Laboratory: Stanford, CA, 2000). The energy position, half width at half-maximum (HWHM), and peak intensity were all allowed to float throughout the fitting process. A function modeling the background was empirically chosen to give the best fit. An acceptable fit reasonably matches both the pre-edge spectrum and its second derivative. In all cases, three acceptable fits with different HWHM (±0.5 fixed from float) backgrounds were acquired over the energy ranges of 7108-7117, 7108-7118, and 7108-7119 eV resulting in a total of nine pre-edge fits per data set, which were averaged to get mean values. Standard deviations for the peak energies and intensities from the pre-edge fits were used to quantify the error.

The EXAFS curve-fitting analysis program OPT in EXAFSPAK (George, G. N. Stanford Synchrotron Radiation Laboratory: Stanford, CA, 2000) was used to fit the EXAFS data. Initial ab initio theoretical phase and amplitude functions were generated by FEFF 7.0[8] using DFT optimized structures for each complex. During the fitting process, the bond distance (R) and the mean-square thermal and static deviation in R (σ^2), which is related to the Debye-Waller factor, were allowed to vary. The threshold energy (E_0), the point at which the photoelectron wave vector k is 0, was also allowed to vary but was constrained as a common value for all components in a given fit. The amplitude reduction factor (S_0^2) was fixed to a value of 1.0 and the coordination numbers (N) were systematically varied to achieve the best fit to the EXAFS data and their Fourier transforms (FTs).
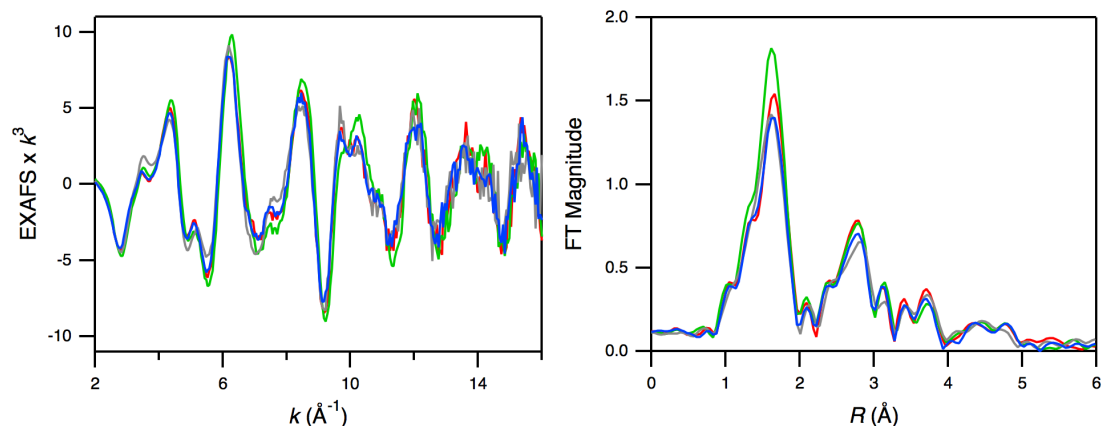

Figure S10. Fe K-edge EXAFS data (left) and non-phase-shift-corrected Fourier transforms (right) of complex **2** (**red**), **3** (**green**), **4a** (**grey**), and **5** (**blue**).
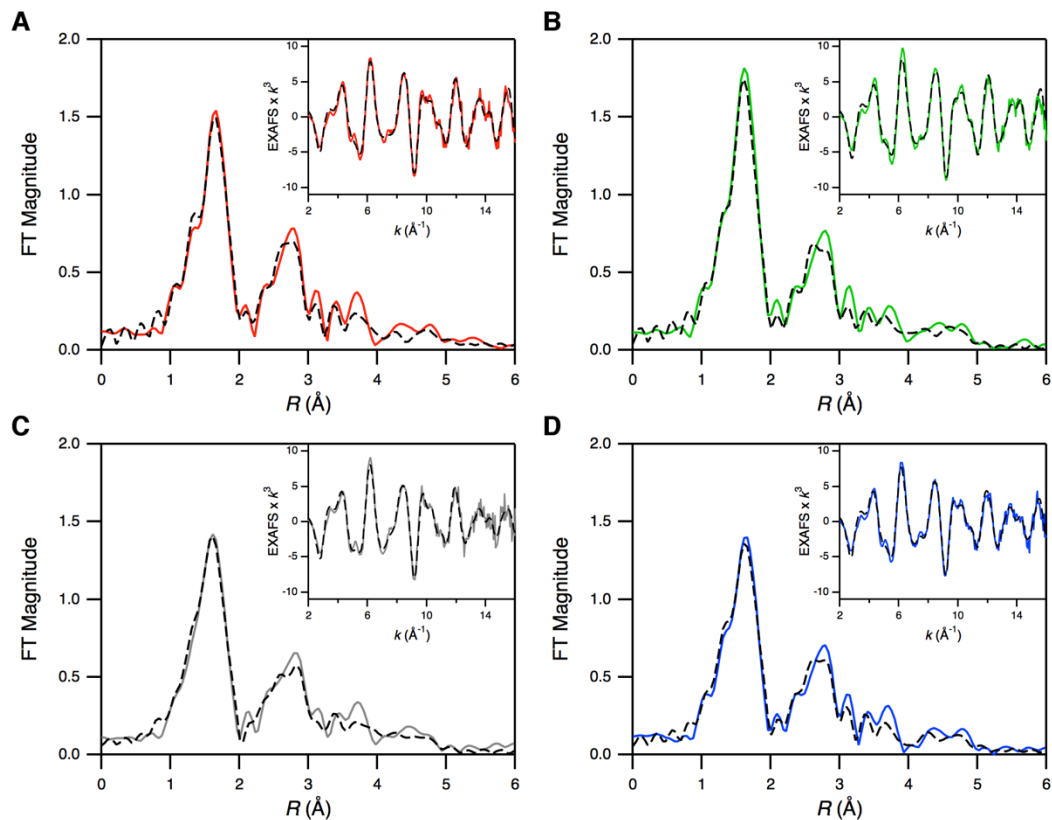
Figure S11. Fe K-edge EXAFS data and non-phase-shift-corrected Fourier transforms of complex (A) **2**, (B) **3**, (C) **4a**, and (D) **5**. Data (—) and fits (---).

Table S1. XAS Pre-edge Energies and Intensities[a]

	peak 1 (eV)	area	peak 2 (eV)	area	peak 3 (eV)	area	total intensity
2	7112.5	6.4					6.4 ± 0.3
3	7111.3	1.0	7112.7	3.6	7113.9	1.2	5.8 ± 0.1
4a	7111.0	0.4	7112.7	3.8	7114.1	2.0	6.2 ± 0.1
5	7112.3	4.8	7114.0	2.6			7.4 ± 0.2

[a]Peak energies are listed at maximum, areas are multiplied by 100 for convenience and comparison to previously published data. To properly model the background of the pre-edge, the additional higher energy feature as part of the edge at 7115.1, 7115.4, 7115.4, and 7115.4 eV was included in the fit of complex **2**, **3**, **4a**, and **5**, respectively. Total intensity is the sum of the areas but does not include the highest energy feature of any fit. Error values are calculated from total intensity deviations across all nine fits.

Table S2. EXAFS Fitting Results

2						**3**					
CN/Path		$R(Å)^a$	$\sigma^2(Å^2)^b$	$\Delta E_0(eV)$	F^c	CN/Path		$R(Å)^a$	$\sigma^2(Å^2)^b$	$\Delta E_0(eV)$	F^c
1	Fe-O/N	1.88	283	-4.55	0.24	6	Fe-N/O	1.99	269	-2.48	0.23
5	Fe-N/O	2.01	182			8	Fe-C	3.03	221		
8	Fe-C	3.03	193			4	Fe-C	3.37	529		
4	Fe-C	3.39	326			8	Fe-C	4.27	430		
8	Fe-C	4.28	360			16	Fe-N-C^d	4.33	430		
16	Fe-N-C^d	4.32	360			8	Fe-C-C	4.91	280		
8	Fe-C-C	4.90	323								

S13

4a					5				
CN/Path	$R(\text{Å})^a$	$\sigma^2(\text{Å}^2)^b$	$\Delta E_0(\text{eV})$	F^c	CN/Path	$R(\text{Å})^a$	$\sigma^2(\text{Å}^2)^b$	$\Delta E_0(\text{eV})$	F^c
1 Fe-O/N	1.92	163	-3.45	0.28	1 Fe-O/N	1.90	357	-3.95	0.24
5 Fe-N/O	2.03	267			5 Fe-N/O	2.01	253		
8 Fe-C	3.04	295			8 Fe-C	3.03	248		
4 Fe-C	3.38	383			4 Fe-C	3.40	367		
8 Fe-C	4.27	325			8 Fe-C	4.30	596		
16 Fe-N-C^d	4.32	325			16 Fe-N-C^d	4.34	596		
8 Fe-C-C	4.90	313			8 Fe-C-C	4.91	334		

^{a}The estimated standard deviations in R for each fit are ±0.02 Å. ^{b}The σ^2 values are multiplied by 10^5. ^{c}The error (F) is given by $[\Sigma[(\chi_{obsd} - \chi_{calcd})^2 k^6]/\Sigma[(\chi_{obsd})^2 k^6]]^{1/2}$. $^d\sigma^2$ for the multiple scattering path is linked to that of the corresponding single scattering path. CN is coordination number. The error in coordination number is 25% and that in the identity of the scatterer Z is ±1.

Fe EXAFS.

The k^3-weighted Fe K-edge EXAFS data and corresponding FTs of complex **2**, **3**, **4a**, and **5** are compared in Figure S10 and their fits and fitting parameters are shown in Figure S11 and Table S2, respectively. The EXAFS beat pattern and intensity are very similar to one another indicating that the complexes have similar structural environments around the Fe(III) center. While the first backscattering shells for complex **2**, **4a**, and **5** were fit best using one short Fe-O/N and five longer Fe-N/O, for complex **3** a split in the first shell gave either unreasonable σ^2 values or the difference in distances between the different paths less than the resolution of the data. The small increase in the EXAFS intensity of complex **3**, which is also reflected in the increase of the first-shell FT peak, is accounted for the non-split six-coordinate first shell (Table S2). The second-shell FT peak in the $R = 2 – 3.5$ Å range was fit with the porphyrin pyrrole α-C and *meso*-C single scattering (SS) components. The intensity in the $R = 3.5 – 5$ Å range was fit with SS and multiple scattering contributions from the pyrrole β- and γ-C atoms.
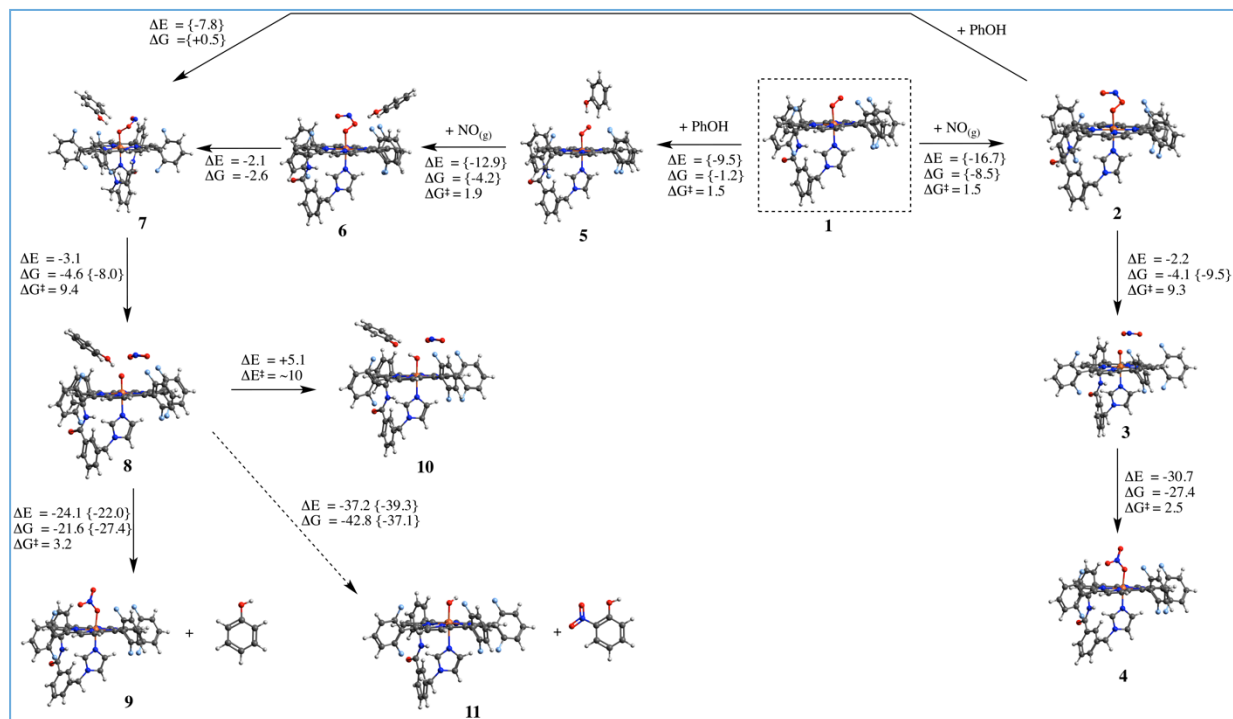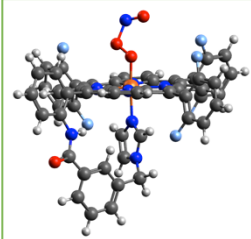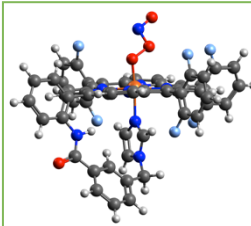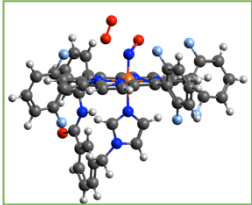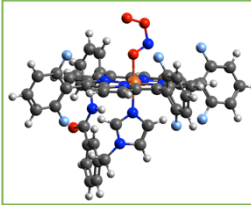
VI. DFT Calculations

Figure S12. Summary of overall thermodynamics calculated using DFT, including structures with and without phenol. Note that the computational model used unsubstituted phenol, while [2,4]DTBP was used experimentally.

Table S3. Optimized DFT PN Conformations

Structures

ΔG (kcal/mol) & Description	0 **O**-O-N=O (*cis*)	+3.17 **O**-O-N=O (*trans*)	-0.41 **O**=N-O-O	+22.11 **O**=N-O-O
Fragment		Fe, OONO, P^{Im}	Fe, NO, P^{Im}, OO	Fe, ONOO, P^{Im}
Charge	1.302331, -0.445844, -0.856487	1.295053, -0.415510, -0.879543	1.186245, -0.095484, -0.849283, -0.241479	1.275606, -0.526639, -0.748968
Spin	0.864879, 0.176482, -0.041361	0.879202, 0.168794, -0.047996	-0.060345, -.125239, -0.002097, 1.187681	0.801722, 0.206911, -0.008632

VII. References:

1. (a) Li, Y.; Sharma, S. K.; Karlin, K. D. *Polyhedron* **2013,** *58*, 190-196; (b) Garcia-Bosch, I.; Sharma, S. K.; Karlin, K. D. *J. Am. Chem. Soc.* **2013,** *135*, 16248-16251.
2. (a) Jankowski, J. J.; Kieber, D. J.; Mopper, K. *Photochem. Photobiol.* **1999,** *70*, 319-328; (b) Otten, D. E.; Petersen, P. B.; Saykally, R. J.,*Chem. Phys. Lett.* **2007,** *449*, 261-265.
3. Melanson, J. E.; Lucy, C. A.,*J. Chromatogr. A* **2000,** *884*, 311-316.
4. (a) Ghiladi, R. A.; Kretzer, R. M.; Guzei, I.; Rheingold, A. L.; Neuhold, Y.-M.; Hatwell, K. R.; Zuberbuehler, A. D.; Karlin, K. D., *Inorg. Chem.* **2001,** *40*, 5754-5767; (b) Kopf, M.-A.; Neuhold, Y.-M.; Zuberbuehler, A. D.; Karlin, K. D.,*Inorg. Chem.* **1999,** *38*, 3093-3102; (c) Karlin, K. D.; Nanthakumar, A.; Fox, S.; Murthy, N. N.; Ravi, N.; Huynh, B. H.; Orosz, R. D.; Day, E. P. *J. Am. Chem. Soc.* **1994,** *116*, 4753-4763.
5. Sharma, S. K.; Kim, H.; Rogler, P. J.; A. Siegler, M.; Karlin, K. D. *J. Biol. Inorg. Chem.* **2016,** *21*, 729-743.
6. Tenderholt, A.; Hedman, B.; Hodgson, K. O., *AIP Conf. Proc.* **2007,** *882* (X-Ray Absorption Fine Structure (XAFS13)), 105-107.
7. Westre, T. E.; Kennepohl, P.; DeWitt, J. G.; Hedman, B.; Hodgson, K. O.; Solomon, E. I. *J. Am. Chem. Soc.* **1997,** *119*, 6297-6314.
8. Rehr, J. J.; Albers, R. C. *Rev. Modern Phys.* **2000,** *72*, 621-654.